Journal of the European Ceramic Society 17 (1997) 819–829

PII: S0955-2219(96)000115-X
0955-2219/97/$17.00

Microstructure Blocking Effects Versus Effective Medium Theories in YSZ

M. Kleitz[a] & M. C. Steil[b]

[a]Laboratoire d'Electrochimie et de Physicochimie des Materiaux et des Interfaces, INPG and CNRS, BP 75, 38402 Saint-Martin d'Hères, France
[b]Laboratoire de Ceramiques Speciales, Centre SMS, ENS des Mines de Saint-Etienne, 42023 Saint-Etienne Cedex 2, France

(Received 22 March 1996; revised version received 3 June 1996; accepted 11 June 1996)*

Abstract

Analogies and differences between the experimental electrical responses of pores and Al_2O_3 inclusions in YSZ and the corresponding predictions by the basic Effective Medium Theories are examined. It is shown that under restricted conditions, the EMT predicts a 'two semicircle' impedance diagram for a composite. Systematic variations of the EMT model parameters demonstrate that, over fairly wide variation intervals, each semicircle can be viewed as a characteristic response of the corresponding component altered by the presence of the other. A comparison with the experimental properties reveals marked differences. Specific experimental features such as the disappearance of the blocking process when the matrix conductivity becomes sufficiently high or the influence of the inclusion grain size on the magnitude of the corresponding semicircle cannot be explained by the EMT. Numerical calculations applied to real cases clearly show that the blocking process semicircle is an additional feature with respect to the EMT predictions. It has been interpreted as experimental evidence for a distortion of the current lines by the microstructure defects. It is a specific property of low-conductivity materials. © *1997 Elsevier Science Limited. All rights reserved.*

1 Introduction

Since the pioneering work of Bauerle,[1] there has been a continuous debate on the models describing the electrical response of the grain boundaries in zirconia-based materials and similar oxide ion conductors. Depending on the way the Impedance Spectroscopy (IS) data are processed, the various models put forward have been classified into 'series' and 'parallel' models also called 'chemical' and 'geometrical' models.[2]

Another basic problem stems from the complexity of the electrical network which connects the grains in a real sintered body. According to Van Dijk and Burggraaf,[3] this should not obscure the characterization of the grain boundaries themselves since a calculation based on a brick layer connection shows that, with appropriate density coefficients, the behaviour of the overall network is similar to that of a single grain boundary.

In fact, many reported impedance diagrams are very simple and can be resolved accurately. Key parameters here are the chemical purity and the microstructure homogeneity of the sample.

Recent results[4–6] have shown that cracks, pores and second-phase inclusions which here will be called Microstructure Defects (MD) behave very similarly to the grain boundaries, in Yttria Stabilised Zirconia (YSZ). A conclusion from these observations is that any model for the grain boundaries should also explain the electrical behaviour of these microstructure defects. Among the specific experimental features which characterize all the MDs is the quasi-parallelism of the logarithmic variations of the MD semicircle conductance and that of the matrix, in the medium temperature range. This feature, and others[6] have led us to develop a parallel model[4] which views the MDs as blockers which statistically immobilize a fraction of the matrix charge carriers, because of strong distortions of the current lines around them. This would be a particular property of matrices with fairly low conductivities. It has not been observed for conductivities of the order of 1 S cm^{-1}, for instance, and frequently disappears at high temperature, when the matrix conductivity gets high enough.

*Text of a lecture presented at the 4th European Ceramic Society Conference, Abstract # ELE-CN-L01, Riccione (I), Oct. 1995.

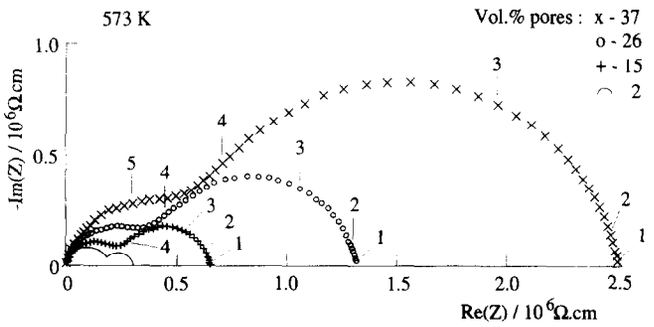

Fig. 1. Impedance diagrams of porous YSZs. Pore diameter of about 0·5 μm. On these diagrams and the following: the number 1, 2, etc indicate the $\log_{10}$ of the measuring frequency; the data are normalized to a geometrical factor equal to 1.

The availability of new data on porous materials and composites offers us an opportunity to critically examine a third approach based on the Effective Medium Theories (EMT). This approach has already been examined by Brailsford and Hohnke[7] and Bonanos *et al.*[8] for the grain boundary response. In this case, as shown by Fricke,[9] the peculiar shape of the grain boundaries requires the use of empirical shape factors which cannot be estimated with any certainty. With porous materials and composites, the application of the EMT equations should be more straightforward and sound as these MDs can reasonably be viewed as spheroids. The main purpose of this paper is to compare the EMT predictions with our experimental diagrams of pores and Al_2O_3 inclusions in YSZ.

For the sake of simplicity we will henceforth call the pores and the Al_2O_3 inclusions by the generic term 'inclusion'. To stay close to the common usage, we will also present the data in their impedance form (Z diagram) instead of their admittance form (Y diagram) which would be more consistent with our model.[4]

2 Experimental Electrical Responses of Inclusions in YSZ

The following figures show examples of experimental 'inclusion' semicircles.

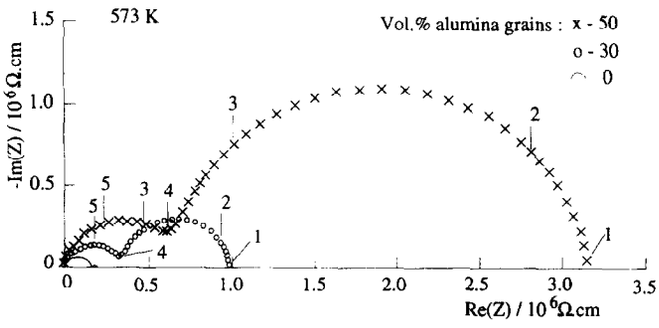

Fig. 2. Impedance diagrams of Al_2O_3/YSZ composites. Alumina grain size of about 1 μm.

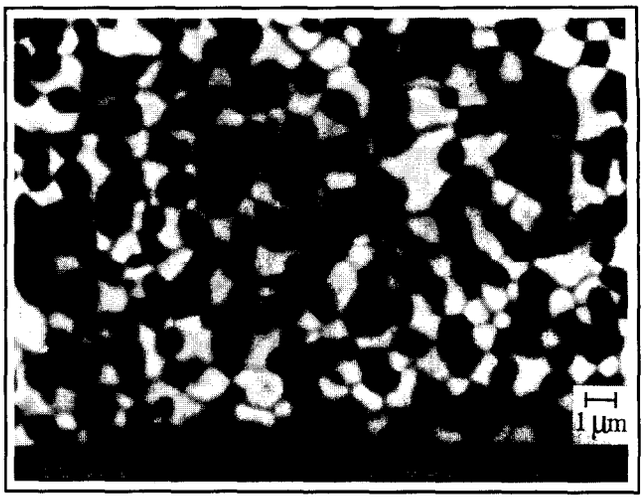

Fig. 3. Micrography of an Al_2O_3/YSZ composite (50 vol% Al_2O_3).

Figure 1 shows diagrams of pores in samples of YSZ 8 mol% (TZ8Y, Tosoh, Japan) isostatically pressed under 400 MPa and sintered at various temperatures for 2 h (experimental details to be published elsewhere).

Figure 2 shows diagrams of Al_2O_3/YSZ composites (TZ8Y from Tosoh and Al_2O_3 AES12 from Sumitomo, Japan) mixed by attrition milling (350 rpm, 4 h) isostatically pressed under 400 MPa and sintered at 1500°C for 2 h. (The other experimental conditions are similar to those of Ref. 12.) A typical micrograph of these samples is given in Fig. 3.

The model and circuit we refer to, to describe the blocking process, are sketched in Fig. 4. According to the reference circuit, these diagrams are better resolved in their admittance forms (Fig. 5) which directly give a parameter $\Sigma_{blocked}$ proportional to the number of blocked charge carriers and Σ_{bulk} which is proportional to the total number of charge carriers in the material.

$$\Sigma_{bulk} = \Sigma_{blocked} + \Sigma_{dc} \quad (1)$$

Note that, when the volume density of MDs is very small, Σ_{bulk} is equal to that of a single crystal of the same composition. This is usually the case

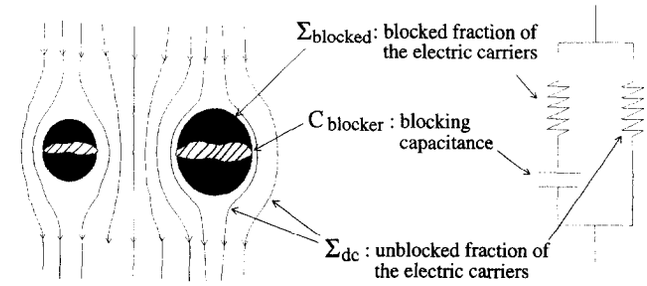

Fig. 4. Model and equivalent circuit showing the distortion of the conduction paths around insulating inclusions and the resulting 'blocked' zones. (This model describes only the blocking process. The capacitance in parallel with the whole circuit which is responsible for the high frequency relaxation has been omitted for simplicity.)

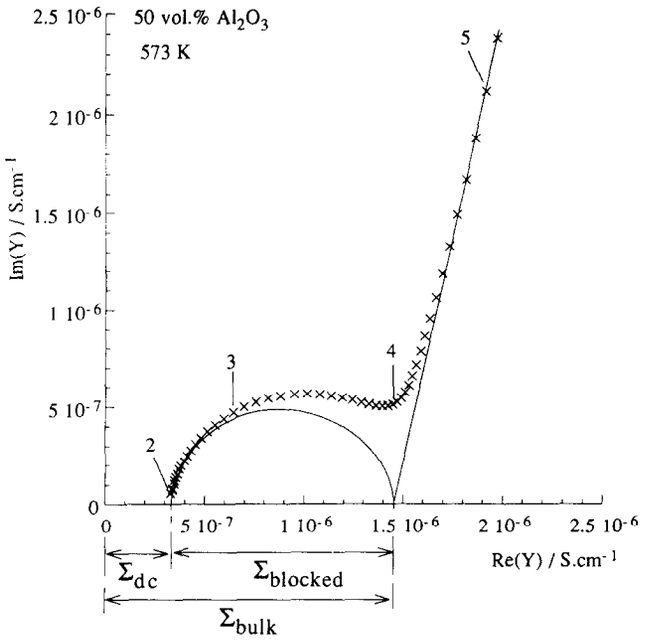

Fig. 5. Typical admittance diagram of an Al_2O_3/YSZ composite and definition of the parameters.

with grain boundaries and cracks, but not with large concentrations of pores or inclusions. The variations in amplitude of the high frequency semicircles in Figs 1 and 2 clearly show this.

The magnitude of the blocking process can be expressed by the a-dimensional blocking factor α_R (for more details, see Ref 4):

$$\alpha_R = \Sigma_{blocked}/\Sigma_{bulk} \quad (2)$$

Figures 6 to 8 shows examples of variation laws which are regarded as specific to the blocking process and which will be compared to the EMT predictions.

Figure 6 shows the quasi-parallelism, in the medium temperature range, between the logarithmic variations of Σ_{bulk} and $\Sigma_{blocked}$ with the tempera-

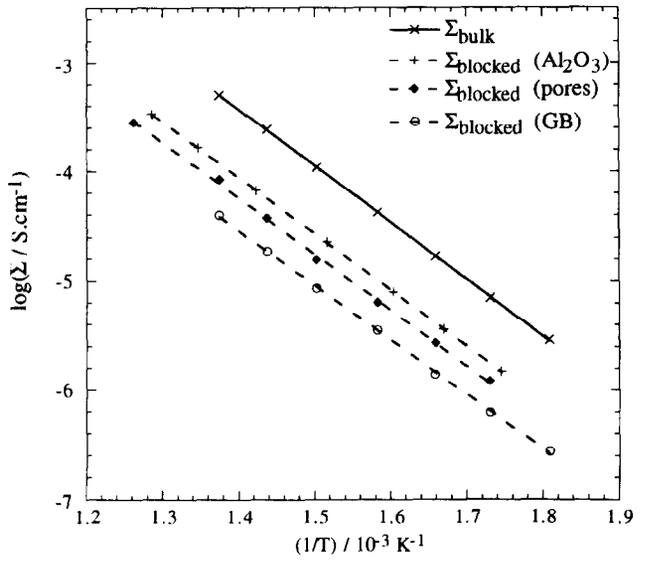

Fig. 6. Arrhenius diagram of the: bulk conductivity of dense YSZ; grain boundary conductivity (GB); blocked conductivity of a porous sample (40 vol% of pores); blocked conductivity of an Al_2O_3/YSZ composite (70 vol% alumina).

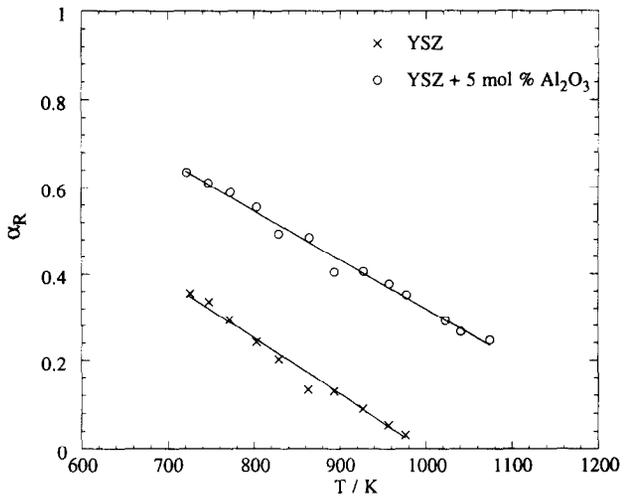

Fig. 7. Decrease of the blocking factor with temperature of a dense YSZ and an Al_2O_3/YSZ composite (Ref. 4).

ture, for grain boundaries (GB), pores and Al_2O_3 inclusions. The bulk conductivity which is the reference in this figure and the grain boundary conductivity were determined from the diagrams of a dense sample prepared from the same TZ8Y powder isostatically pressed under 400 MPa and sintered at 1500°C for 2 h. Similar parallelisms have been observed with other materials, for variations as a function of the doping of the matrix or the equilibrium oxygen pressure.[10–12] That is the type of observation which led us to assign $\Sigma_{blocked}$ to a part of the matrix (in other words, to the 'blocked' zones shown in Fig. 4).

Above a certain critical temperature, which means above a certain matrix conductivity, the blocking effect decreases until a complete disappearance of the corresponding semicircles.[4] Figure 7 shows such a decrease (measured by α_R) as the temperature of the material increases.

Figure 8 shows that, at constant Al_2O_3 volume content (20%), the size of the inclusion grains has a marked effect on the second component semicircle. A more detailed investigation[13] has shown that the size of this semicircle increases with the average surface of the blocking MDs, perpendicular to the average electric field applied to the material and that its relaxation frequency increases

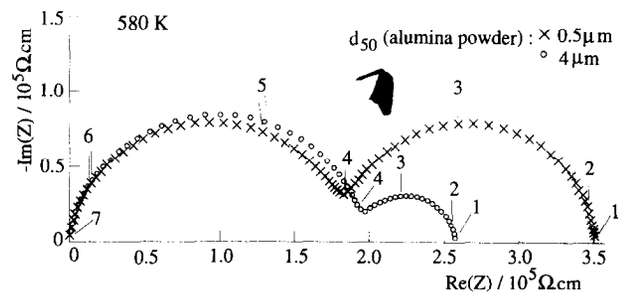

Fig. 8. Influence of the grain size on the impedance diagrams of Al_2O_3/YSZ composites (20 vol% of alumina, same preparation conditions as in Ref. 12).

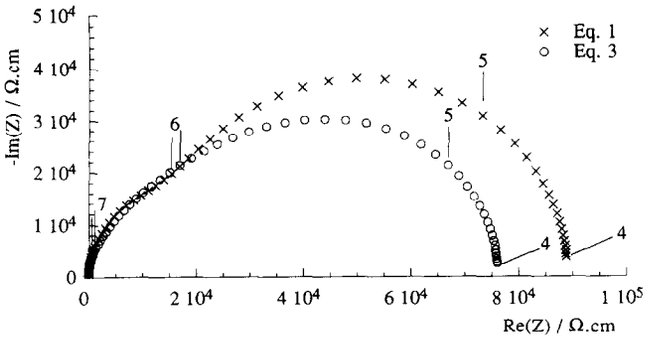

Fig. 9. Comparison of the theoretical diagrams deduced from the Maxwell–Garnett equation (eqn (3)) and the Bruggeman equation (eqn (5)). $\sigma_m = 6 \times 10^{-6}$, $\epsilon_m = 60$, $\sigma_{in} = 6 \times 10^{-5}$, $\epsilon_{in} = 11$, $v_{in} = 0{\cdot}3$.

with the average thickness of these MDs, parallel to the field.

3 Effective Medium Theories

The electrical behaviour of composite materials has been the subject of numerous developments since the end of the 19th century. It is beyond the scope of this paper to review all this work. Readers interested are referred to the review papers by Landauer,[14] McLachlan *et al.*[15] and Bergman and Stroud.[16]

For our purpose we will mostly use the Maxwell–Garnett basic equation which is valid for spheroïd inclusions, as did Brailsford and Hohnke,[7] Bonanos *et al.*[8] and Bonanos and Lilley.[17] The validity of this use has been re-demonstrated by Stroud *et al.*[18] on the basis of Bergman's approach (see below). This equation can be written as:

$$Y_{comp} = Y_m \frac{2Y_m + Y_{in} - 2v_{in}(Y_m - Y_{in})}{2Y_m + Y_{in} + v_{in}(Y_m - Y_{in})} \quad (3)$$

It gives the composite admittance Y_{comp} as a function of the matrix admittance Y_m, the inclusion admittance Y_{in} and the volume fraction of the inclusions v_{in}. The admittances will be written in the form

$$Y_j = \sigma j + i\,\omega\,\epsilon_j\epsilon^\circ \quad (4)$$

where σj is the j component conductance (j = m or in), ϵ_j its relative permittivity and ω the pulsation of the electric signal.

This equation is regarded as fully valid for dilute composites in which the inclusion grains do not electrically interfere. Its validity limit, in terms of inclusion concentration, has never been clearly evaluated. It is frequently used up to fairly high concentrations. The derivation we will develop will not be based on quantitative determinations (except in one case), but only on general trends and qualitative variation laws. Therefore, the errors which might result from going somewhat beyond the validity limit should not be misleading for our purpose.

The above equation is asymmetrical in the sense that the two components do not play symmetrical roles.

Bruggeman[19] has generalized this conventional EMT approach and given the following symmetrical equation which has been used, for instance, by Tomkiewicz and Aurian-Blajeni:[20]

$$v_1 \frac{\epsilon_1 - \epsilon_{comp}}{\epsilon_1 + 2\epsilon_{comp}} + v_2 \frac{\epsilon_2 - \epsilon_{comp}}{\epsilon_2 + 2\epsilon_{comp}} = 0 \quad (5)$$

where the ϵ's are the complex permittivities which include the conductivity contributions. The subscripts 1 and 2 refer to the two components. It is applicable over a wider range of concentrations. Figure 9 compares a diagram deduced from it to the corresponding one calculated from the basic equation, eqn (3). Quantitatively the difference is significant, but qualitatively such differences will not alter the conclusions drawn below.

In the development of the EMT, the other important step towards generalization is due to Bergman[21,22] who introduced an analytical expression with a specific pole structure for describing the complex dielectric behavior of the composites. For materials with properties close to ours, it was implemented by Stroud *et al.*,[18] for instance.

Recently McLachlan[23] who has mostly investigated the dc conductivity behaviors of composites proposed an equation which accurately describes the electrical behavior of a material in the vicinity of the percolation threshold of one of its components. The concentrations we will deal with will remain fairly distant from any percolation threshold (in the Al_2O_3/YSZ composites examined, it was estimated[5] to be close to 70 vol% Al_2O_3) and the use of such an elaborated equation would be complicated needlessly.

4 Theoretical Diagrams and Variation Laws

As a function of the impedance ratio R_Z of the components:

$$R_Z = Z_{in}/Z_m \quad (6)$$

the basic eqn (3) can be written (for both components: $Z_i = 1/Y_i$):

$$Z_{comp} = Z_m \frac{(1 - v_{in}) + (2 + v_{in})\,R_Z}{(1 + 2v_{in}) + 2\,(1 + v_{in})\,R_Z} \quad (7)$$

or

$$Z_{comp} = Z_m \times S(R_Z) \quad (8)$$

This way of writing it shows that the impedance diagrams of a composite (with a fairly low con-

centration of inclusions) can be regarded as equal to that of the matrix (Z_m) which is a single semicircle, altered by a shape factor $S(R_Z)$ which only depends on the impedance ratio R_Z.

Our main objective will be to demonstrate that the theoretical two-semicircle diagrams predicted by the EMT, if any, match or do not match our experimental data. Therefore, the first step will be a search for values of R_Z which make the shape factor 'strong enough' to alter the matrix single semicircle into a two-semicircle diagram.

The hyperbolic expression of the shape factor (eqns (7) and (8)) indicates that it tends towards constant values when R_Z becomes large or small. We can then restrict our search to an interval of medium R_Z values. Outside this interval the situation prevailing at the corresponding interval boundary will remain unchanged. (See results below.)

Quantitatively, our search can be limited to the variation domain defined by the double condition.

$$10^{-2} < |R_Z| < 10^2 \tag{9}$$

The results obtained and reported below will confirm the validity of this condition. $|R_Z|$ is approximately equal to the conductivity ratio σ_m/σ_{in} at low frequencies and to the permittivity ratio ϵ_m/ϵ_{in} at high frequencies. Taking into account that the variations of the permittivities can be limited to the following fairly narrow interval, with the conventional materials forming our composites:

$$1 \leq \epsilon_j \leq 100 \tag{10}$$

the above double condition can be converted into the set of conditions:

$$10^{-2} < \sigma_m/\sigma_{in} < 10^2 \tag{11}$$

$$10^{-2} < \epsilon_m/\epsilon_{in} < 10^2 \tag{12}$$

The fact that only the conductivity and permittivity ratios are decisive parameters for our derivation allows us to arbitrarily choose σ_m and ϵ_m and then simply vary σ_{in} and ϵ_{in} to cover the variation domain defined by the previous conditions.

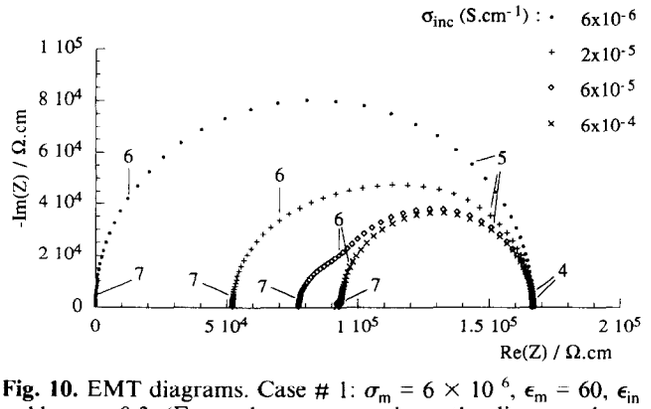

Fig. 10. EMT diagrams. Case # 1: $\sigma_m = 6 \times 10^{-6}$, $\epsilon_m = 60$, $\epsilon_{in} = 11$, $v_{in} = 0{\cdot}3$. (For a clearer comparison, the diagrams have been shifted to obtain a coincidence of their low frequency points.)

To obtain theoretical diagrams comparable to the experimental data of Figs 1 and 2, initially, we will take for σ_m and ϵ_m the conductivity and permittivity values of the YSZ investigated at 573 K, respectively: 6×10^{-6} S cm^{-1} and 60. In a first case, we will also select for the inclusion permittivity value that of alumina: 11.

These conditions are summarized below.

Case # 1: $\epsilon_{in} < \epsilon_m$

$$\sigma_m = 6 \times 10^{-6} \text{ S cm}^{-1}$$

$$\epsilon_m = 60$$

$$10^{-7} < \sigma_{in} < 10^{-3} \text{ S cm}^{-1}$$

$$\epsilon_{in} = 11$$

$$v_{in} = 0{\cdot}3 \text{ (i.e. 30 vol\%)}$$

Figure 10 shows that eqn (3) can give a two-semicircle diagram, under the conditions defined above.

The systematic variations of the conductivity (and the dielectric) parameters that we have carried out have furthermore shown that:

— When ϵ_{in} is smaller than ϵ_m, a two-semicircle diagram is obtained only when:

$$\sigma_{in} > \sigma_m \tag{13}$$

— With respect to the matrix-specific semicircle, the second semicircle appears on the high frequency side. This is consistent with the expectations because the specific relaxation F^0_{in} of the inclusion material:

$$F^0_{in} = \frac{\sigma_{in}}{2\,\pi\,\epsilon_{in}\,\epsilon^0} \tag{14}$$

is higher than that of the matrix.

— As the inclusion conductivity increases, the high frequency semicircle decreases in magnitude. At the high conductivity boundary of the variation domain, it practically vanishes (Fig. 10). Outside the variation domain, a more careful examination of the diagrams indicates that a second semicircle still exists, for conditions not too distant from this boundary. However, it is much smaller than the main semicircle and the situation is undoubtedly different from that of the experimental results with which we want to establish similarities. This tiny second semicircle may show up more clearly in other representation modes, for instance on admittance diagrams.[8]

— As the inclusion conductivity decreases and gets close to the matrix conductivity value, the overlapping between the two semicircles increases until there is a complete fusion into a single semicircle. On further decrease of this conductivity the shape of the diagram remains unchanged.

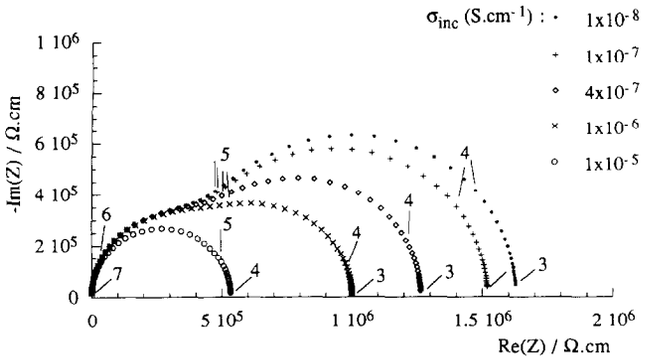

Fig. 11. EMT diagrams. Case # 2: $\sigma_m = 1 \times 10^{-6}$, $\epsilon_m = 6$, $\epsilon_{in} = 60$, $v_{in} = 0{\cdot}3$.

To obtain a second semicircle, on the low frequency side with respect to the specific matrix semicircle, which would correspond to our experimental results, the permittivity of the inclusion needs to be higher than that of the matrix. With the YSZ matrix examined above, that would be the case if the inclusion had a permittivity of 300, for instance. To illustrate this situation with more realistic parameters, we have selected the following variation domain which could correspond to inclusions of zirconia, in a conducting glass at medium temperatures, for instance.

Case # 2: $\epsilon_{in} > \epsilon_m$

$$\sigma_m = 1 \times 10^{-6}\ \text{S cm}^{-1}$$

$$\epsilon_m = 6$$

$$10^{-4} < \sigma_{in} < 10^{-8}\ \text{S cm}^{-1}$$

$$\epsilon_{in} = 60$$

$$v_{in} = 0{\cdot}3$$

In this case, two-semicircle diagrams are obtained (Fig. 11) when:

$$\sigma_{in} < \sigma_m \qquad (15)$$

— Here, the inclusion semicircle does appear on the low frequency side with respect to the matrix semicircle (which also makes sense for a reason similar to that invoked in case # 1).

— The evolutions are similar to those previously observed when the conductivities get close to each other, then the overlapping gradually increases.

— On the other hand, they are significantly different at the other domain boundary. When σ_{in} gets close to $10^{-2}\sigma_m$, the diagram stabilizes into a two-semicircle picture (Fig. 11). For values much smaller than this limit, the diagram is the same, even for a fully insulating inclusion ($\sigma_{in} = 0$).

5 Variations of the Theoretical Semicircle Parameters

To be consistent with the qualitative observations made above regarding the location of the 'second' semicircle with respect to the 'main' one, we will call this main loop the matrix semicircle and the second one the inclusion semicircle. The conclusions of this section will confirm the validity of these identifications.

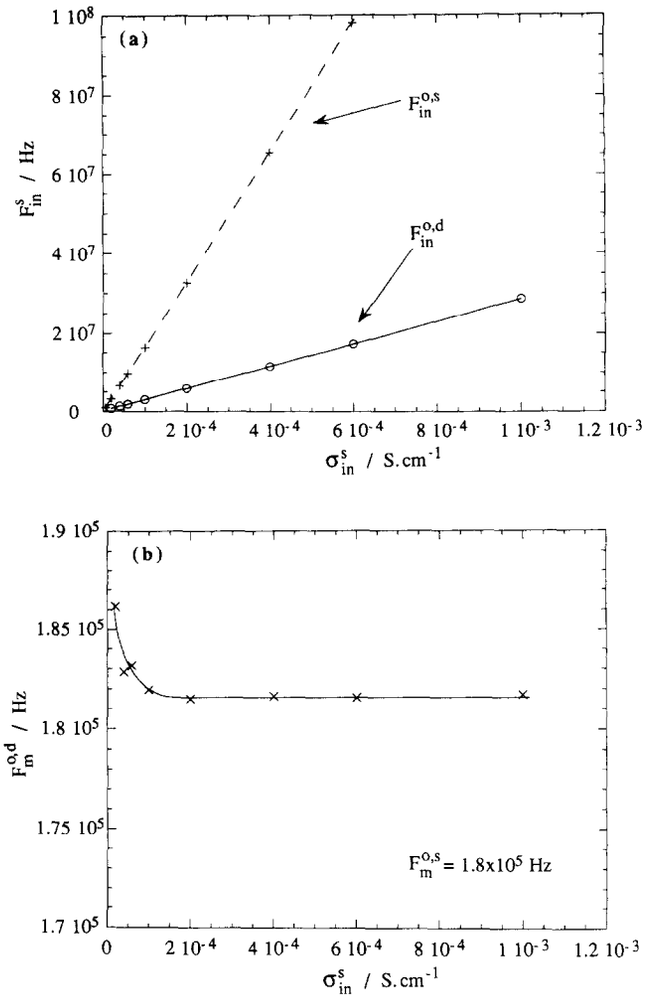

Fig. 12. Parameters of the EMT diagrams shown in Fig. 10. (a) Inclusion relaxation frequencies (the line F^{as}_{in} given for comparison, shows the specific relaxation frequencies of the single-phased inclusion). (b) Matrix relaxation frequencies.

In the following part of the paper, the parameter values deduced from the diagrams will be identified by a superscript 'd'. To contrast with them, a superscript 's' will identify the specific values assigned to the component parameters. For instance, σ^d_{in} will be a conductivity deduced from the diameter of a second semicircle. In case # 1, ϵ^s_{in} is equal to 11.

In the variation domains defined above (cases # 1 and 2), we have gradually varied σ^s_{in} and resolved the corresponding diagrams into two semicircles (NLS curve fitting program developed for Hydro-Quebec). Various results stressed in this manuscript suggest viewing the theoretical semicircles as characteristic responses of the components, altered by the presence of the other (see the proportionality laws below, for instance). Accordingly, we have resolved the theoretical diagrams by referring to a

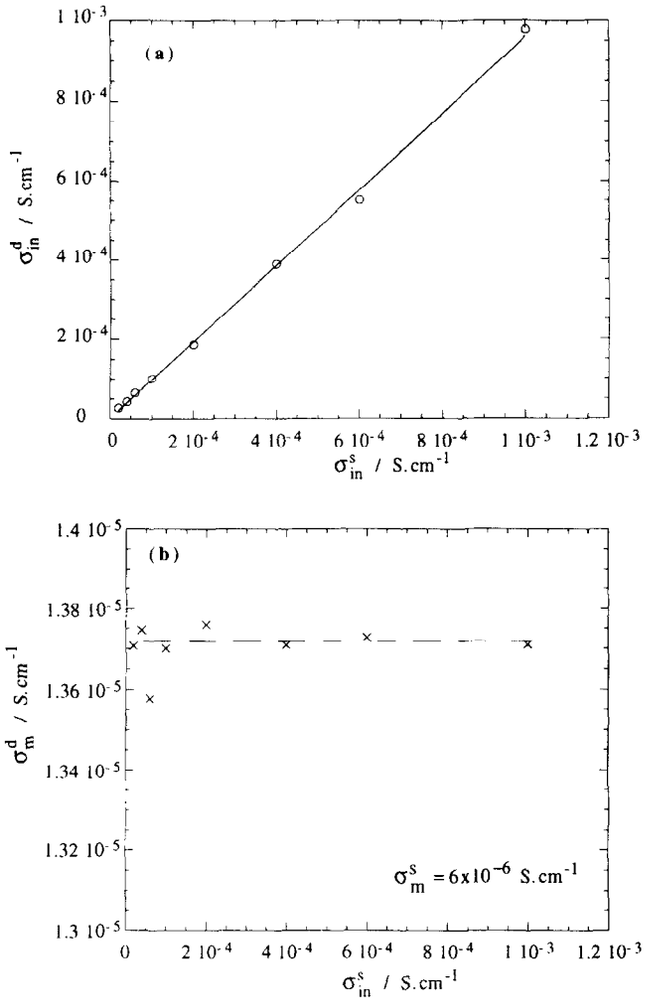

Fig. 13. Conductivities deduced from the EMT diagrams shown in Fig. 10: (a) inclusion conductivity, (b) matrix conductivity.

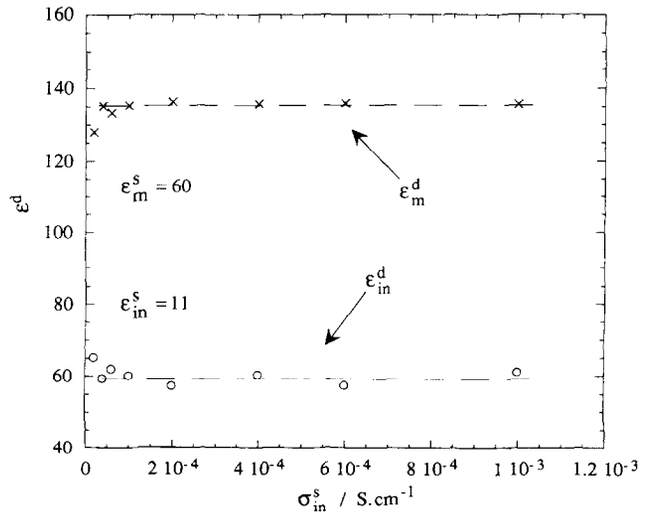

Fig. 14. Permittivities deduced from the model diagrams shown in Fig. 10.

series circuit. This gives useful data in a more conventional form and has no incidence on our comparison between the theoretical predictions and the experimental observations (see the conclusion section). The main observations and the variation laws of the semicircle parameters are given below.

First, the component semicircles are always centered on the real axis.

Case # 1

Figures 12 to 14 show the variations as functions of σ^s_{in}, of the matrix and inclusion parameters deduced from the diagrams in Fig. 10.

Figure 12a shows that the inclusion relaxation frequencies remain proportional to its specific value. That of the matrix (Fig. 12b) remains quasi-constant, which means that it also remains proportional to the corresponding specific value.

Figures 13a and b show that the 'diagram' conductivities vary similarly to the relaxation frequencies in that they remain proportional to the specific values (except in a narrow interval of small σ^s_{in}). The calculation of these conductivities raised a problem. From the diagrams one deduces conductances. To obtain conductivities which can be compared to the specific values, it is necessary to normalize them by an appropriate geometrical factor. Ideally, it should take into account the volume fraction v_{in}. For reasons given below, the calculated electrical parameters reported here have only been normalized by the geometrical factor of the sample (which is 1 in this whole derivation). For the data analyzed above, the volume fractions being constant the potential error associated with this procedure should not alter the conclusions.

The dielectric constants (Fig. 14) that we calculated in the same way remain constant as functions of σ^s_{in}. They also stay proportional to the specific values. Their values appear fairly high.

Conclusions which can be drawn from these variation laws are:

— The values of the relaxation frequencies, conductivities and permittivities that are deduced from these theoretical diagrams are markedly altered with respect to the specific values of the components. From an experimental viewpoint, the relaxation frequencies appear to be less dramatically affected. Referring to them would still allow us to identify a given semicircle (i.e. to ascribe it to one of the composite components).

— When the inclusion conductivity varies only the 'diagram' inclusion conductivity varies and the variations are proportional. The relaxation frequency varies accordingly, obeying an equation similar to eqn (14) in which the permittivity is constant:

$$F^{0,d}_{in} = \frac{\sigma^d_{in}}{2\,\pi\,\epsilon^d_{in}\,\epsilon^0} \tag{16}$$

Case # 2

In case # 2 (diagrams of Fig. 11), the variation laws obtained and the conclusions are fairly similar,

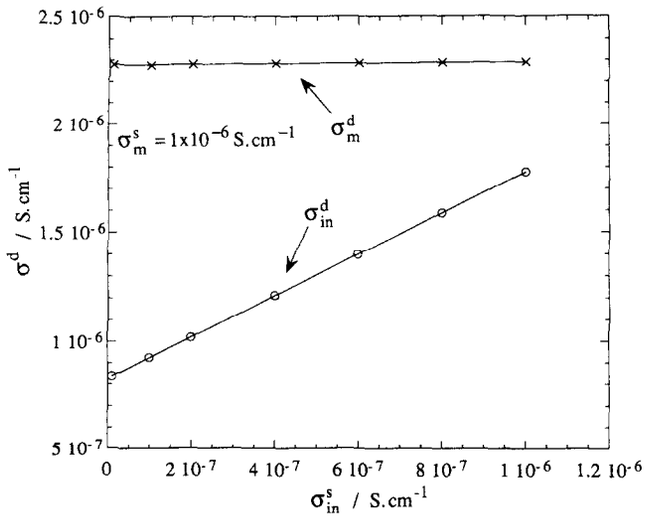

Fig. 15. Conductivities deduced from the model diagrams shown in Fig. 11.

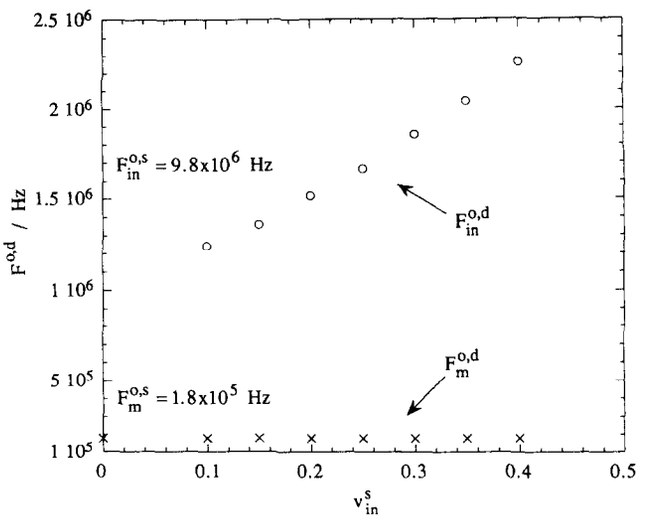

Fig. 17. Influence of the volume fraction of the inclusion on the relaxation frequencies. $\sigma^s_m = 6 \times 10^{-6}$, $\epsilon^s_m = 60$, $\sigma^s_{in} = 10^{-5}$, $\epsilon^s_{in} = 11$.

with the only exceptions that the straight lines describing the variations of the relaxation frequency and the conductivity with σ^s_{in} do not cross the origin (see Fig. 15, for instance). This is relevant to the observation that the inclusion semicircle does not disappear when σ^s_{in} decreases to zero.

Case # 2a: ϵ^s_{in} variable

To confirm the conclusion regarding the proportionalities between the 'diagram' values and the assigned specific values, we also carried out a variation of ϵ^s_{in} at constant σ^s_{in} under conditions similar to case # 2. We obtained a variation of ϵ^d_{in} proportional to that of ϵ^s_{in} (Fig. 16) and σ^d_{in} remains constant, which means proportional to σ^s_{in}.

To characterize these proportionalities, we have examined the effects of the inclusion volume fraction on the parameters, for an intermediate value of σ^s_{in} and under conditions similar to case #1.

Case # 1a: v_{in} variable

$$\sigma^s_m = 6 \times 10^{-6}\ \text{S cm}^{-1}$$

$$\epsilon^s_m = 60$$

$$\sigma^s_{in} = 6 \times 10^{-5}\ \text{S cm}^{-1}$$

$$\epsilon^s_{in} = 11$$

$$0 < v_{in} < 0{\cdot}4$$

Typical variation laws are shown in Figs 17 to 19. The variations are monotonous and simple variation laws could be found.

The first observation is that the matrix relaxation frequency $F^{o,d}_m$ is independent from v_{in}. This further supports the suggestion that relaxation frequencies can be used as indications to identify the corresponding semicircles; it implies that the matrix conductivity and permittivity vary proportionally ($\epsilon^d_m \propto \sigma^d_m$).

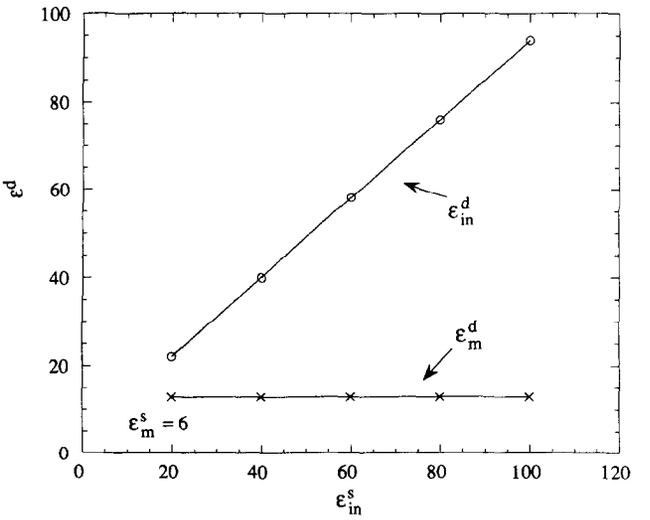

Fig. 16. Influence of the specific permittivity of the inclusion on the permittivities deduced from the diagrams. $\sigma^s_m = 1 \times 10^{-6}$, $\epsilon^s_m = 6$, $\sigma^s_{in} = 1 \times 10^{-7}$, $v_{in} = 0{\cdot}3$.

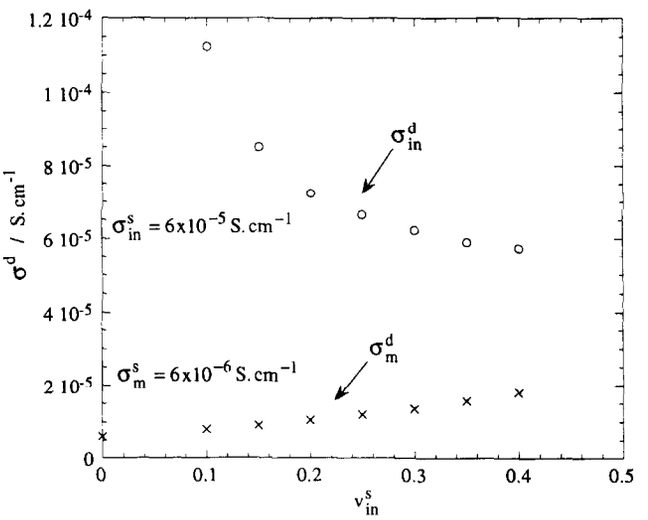

Fig. 18. Influence of the volume fraction of the inclusion on the conductivities deduced from the diagrams. Same electrical parameters as in Fig. 17.

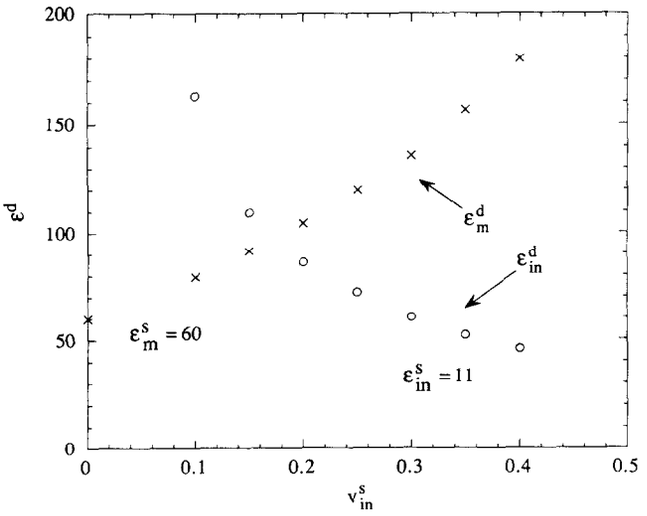

Fig. 19. Influence of the volume fraction of the inclusion on the permittivities deduced from the diagrams. Same electrical parameters as in Fig. 17.

On the other hand, the 'diagram' values for the inclusion relaxation frequency can be markedly different from the specific value of the material $F^{o,s}_{in}$.

The simple correlations which could be established between the calculated electrical parameters and v_{in}, in both cases (# 1 and 2), are the following:

— σ^d_{in} and ϵ^d_{in} vary approximately linearly with $1/v_{in}$,

— σ^d_m and ϵ^d_m obey exp(const $\times$ v_m) laws where v_m is the volume fraction of the matrix. These correlations should be regarded only as indicative, as the use of another EMT equation, such as the Bruggeman equation (eqn (5)) may give slightly different calculated parameters.

The most remarkable observation which can be made is that some of the variation directions may offend common sense. From the data in Fig. 18, for instance, it could be deduced that the part played by the matrix in the overall conductance of the composite increases as its volume fraction decreases! The contribution of the inclusion is also quite surprising, at first glance. It decreases as its volume fraction increases. Under these circumstances, any type of normalization of the diagram parameters, taking into account v_{in} would look arbitrary. That is why we have simply normalized the diagram parameters with respect to the geometrical factor of the sample.

A further set of interesting data can be collected at the low inclusion conductivity boundary of case # 2. We have seen that outside the variation interval (when the specific inclusion conductivity is low enough), the diagram no longer depends on this conductivity. For this purpose, we have selected a very small value for σ^s_{in} (1×10^{-15} S cm^{-1}) which

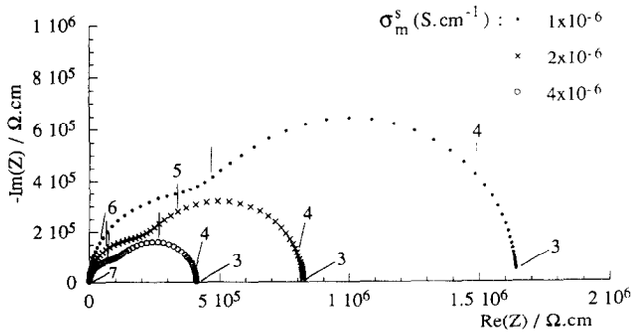

Fig. 20. Influence of the matrix conductivity on the impedance diagrams. Insulating inclusion with a relatively high permittivity. $\epsilon^s_m = 6$, $\sigma^s_{in} = 1 \times 10^{-15}$, $\epsilon^s_{in} = 60$, $v_{in} = 0{\cdot}3$.

corresponds to an insulating inclusion. This situation is fairly close to that of the experimental results reported in Figs 1 and 2, except that here the inclusion dielectric constant is higher than that of the matrix. To stay close, in terms of conductivity, to the conditions of Figs 1 and 2, the specific matrix conductivity was then varied over the following variation interval:

Case # 2b: σ^s_m variable and very low σ^s_{in}

$$6 \times 10^{-6} < \sigma^s_m < 10^{-2} \text{ S cm}^{-1}$$

$$\epsilon^s_m = 6$$

$$\sigma^s_{in} = 1 \times 10^{-15} \text{ S cm}^{-1}$$

$$\epsilon^s_{in} = 60$$

$$v_{in} = 0{\cdot}3$$

The main conclusion here is that the diagram changes homothetically (Fig. 20) with σ^s_m. The logarithmic variations in σ^d_{in} and σ^d_m are parallel (Fig. 21). This is identical to the experimental variations shown in Figs 1 and 2. The dielectric constants are not altered by the variations of σ^s_m

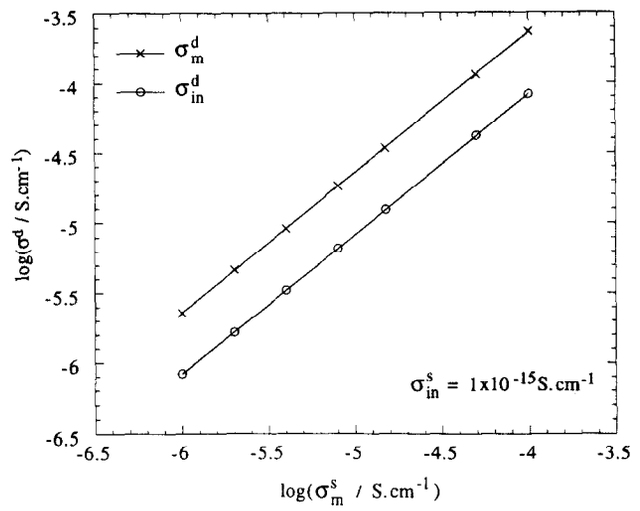

Fig. 21. Influence of the matrix conductivity on the conductivities deduced from the diagrams, under the conditions of Fig. 20.

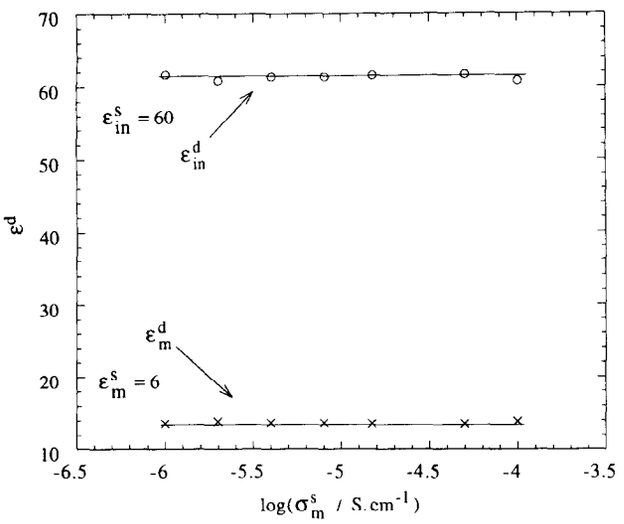

Fig. 22. Influence of the matrix conductivity on the permittivities deduced from the diagrams, under the conditions of Fig. 20.

(Fig. 22). In the case examined, one obtains for the constant values:

$$\epsilon^d_m = 13{\cdot}5$$

$$\epsilon^d_{in} = 61{\cdot}5$$

However, such an ϵ^d_{in} value is significantly different from the usual experimental results which are much bigger, typically of the order of several thousand (7500 in the case of the alumina inclusions shown in Fig. 2).

6 Comparisons with the Experimental Observations

The major difference which in itself would suffice to rule out any explanation of the experimental characteristic features of the MD semicircles by the Effective Medium Theories is the absence of any second semicircle in the theoretical Z diagrams when the inclusions are insulators and their permittivities smaller than that of the matrix, which is in total contrast with the results shown in Figs 1 and 2.

Other significant differences support the conclusion that the EMT cannot describe the features shown in Figs 1 and 2:

— According to the EMT, a key parameter for obtaining a two-semicircle diagram is the value of the σ_m/σ_{in} ratio. The absolute value of the matrix conductivity σ_m on its own is not decisive. Our simulations have shown that two semicircles can indeed be obtained with σ^s_{in} = 1000 S cm^{-1} and σ^s_m = 10 S cm^{-1}, for instance. This is in contradiction with many converging experimental observations which indicate that the MD semicircles do not exist when the matrix conductivity is high enough.

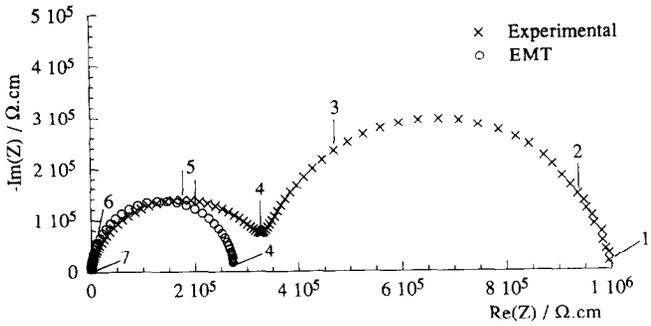

Fig. 23. Comparison between the experimental diagram of an Al_2O_3/YSZ composite (30 vol% of alumina) and the corresponding diagram deduced from eqn (3) (EMT). $\sigma^s_{in} = 6 \times 10^{-6}$, $\epsilon^s_m = 60$, $\sigma^s_{in} = 10^{-10}$, $\epsilon^s_{in} = 11$, $v_{in} = 0{\cdot}3$.

— As recalled in the introduction, it has been experimentally observed that, all the other parameters being kept constant, variations in the matrix conductivity most generally induce 'virtually proportional' variations of the blocked conductances. Variations of this type are predictable only in case # 2, when the inclusion dielectric constant is higher than that of the matrix.

— The EMT do not predict the size effect shown in Fig. 8. This inconsistency is even more striking with samples in which the microstructure defects can be grouped into two families of sufficiently different average diameters (microstructure defects with a bimodal size distribution). Then the experimental Z diagrams exhibit 2 MD semicircles.[4] The EMT do not predict any behavior of this type.

— As mentioned above, the experimental capacitive effects associated with the MD semicircles are frequently enormous, corresponding to equivalent dielectric constants higher than 1000. This observation was already made[24–26] in the mid-sixties, in the petroleum prospection field and was identified as the 'dielectric anomaly of rocks'. The calculations reported above do not indicate that such high capacitive effects are commonly predicted by the conventional EMT equations. (They have been tentatively explained by invoking the presence of highly anisotropic insulating inclusions[25] or other microstructure peculiarities[26].)

To obtain a more quantitative evaluation of the misfit between the EMT predictions and the experimental data, we have calculated the theoretical Z diagrams corresponding to several of our experimental data. Figure 23 shows a typical result: in fact, the theoretical diagram reasonably fits the experimental bulk semicircle, but not the MD semicircle.

This sheds some light on diagrams we have obtained with ZnO/YSZ composites at a medium temperature where both components exhibit somewhat similar conductivities.[12] With this system we could clearly separate three semicircles. The two

high frequency semicircles could be those predicted by the EMT in case # 1 or 2 (unfortunately, a calculation could not be made to verify this assumption because the conductivity of ZnO saturated with ZrO_2 and possibly Y_2O_3 was unknown in our samples).

Conclusion

From this comparison of theoretical diagrams predicted by the Effective Medium Theories and experimental data obtained with YSZ based materials, we can conclude that, most likely, the variations observed for the bulk semicircle, with the pore density or with the concentration in alumina inclusions are those predicted by these Theories. On the other hand, the experimentally observed semicircles associated with the presence of microstructure defects are additional features. They should be regarded as experimental evidence for an additional physical property, specific to low conductivity materials. Recent results by Fleig and Maier[27] obtained by a finite element calculation of the electrical resistance of an imperfect contact confirm that a distortion of current lines can show up on an impedance diagram as an additional semicircle.

When the two components of the composite exhibit fairly similar conductivities and sufficiently different permittivities, the bulk response is likely to be made up of two semicircles.

Acknowledgement

M. C. Steil acknowledges grants from St Etienne's School of Mining and the Brasilian CNPq.

References

1. Bauerle, J. E., Study of solid electrolyte polarization by a complex admittance method. *J. Phys. Chem. Solids*, **30** (1969) 2657–2670.
2. Kleitz, M., Pescher, C. & Dessemond, L., Impedance spectroscopy of microstructure defects and crack characterization. In *Science and Technology of Zirconia*, V, ed. S. P. S. Badwal, M. J. Bannister & R. H. J. Hannink. Technomic Publ., Co., Lancaster–Basel, 1993, pp. 593–608.
3. Van Dijk, T. & Burggraaf, A. J., Grain boundary effects on ionic conductivity in ceramic $Gd_xZr_{1-x}O_{2-x/2}$. *Phys. Stat. Sol. A*, **63** (1981) 229–240.
4. Kleitz, M., Dessemond, L. & Steil, M. C., Model for ion-blocking at internal interfaces in zirconias. *Solid State Ionics*, **75** (1995) 107–115.
5. Steil, M. C., Thevenot, F., Dessemond, L. & Kleitz, M., Impedance spectroscopy analysis of conduction percolation in zirconia–alumina composites. In *Third Euro Ceramics, Vol. 2*, ed. P. Duran & J. F. Fernandez. Faenza Editrice Iberica, San Vincente, Spain, 1993, pp. 271–280.
6. Dessemond, L., Muccillo, R., Henault, M. & Kleitz, M., Electric conduction-blocking effects of voids and second phases in stabilized zirconia. *Appl. Phys.*, **A57** (1993) 57–60.
7. Brailsford, A. D. & Hohnke, D. K., The electrical characterization of ceramic oxides. *Solid State Ionics*, **11** (1983) 133–142.
8. Bonanos, N., Steele, B. C. H., Butler, E. P., Johnson, W. B., Worrel, W. L., Macdonald, D. D. & McKubre, M. C. H., Applications of impedance spectroscopy. In *Impedance Spectroscopy*, ed. J. R. Macdonald. John Wiley & Sons, New York, 1987, pp. 191–237.
9. Fricke, H., The Maxwell–Wagner dispersion in a suspension of ellipsoïds. *J. Phys. Chem.*, **57** (1953) 934–937.
10. Saito, Y. & Maier, J., Ionic enhancement of the fluoride conductor CaF_2 by grain boundary activation using Lewis acids. *J. Electrochim. Soc.*, **142** (1995) 3078–3083.
11. Vangrunderbeek, J., Luyten, J., Kuypers, S., Hendrix, W. & De Schutter, F., Impedance spectroscopy study of superplastic 0·3 mol% CuO modified 3YTZP oxygen sensor material. *Electrochim. Acta*, **38** (1993) 2099–2102.
12. Kleitz M., Djurado, E., Robert, P. O., Steil, M. C. & Thevenot, F., Impedance spectroscopy analysis of the electric behavior of ceramic composites. In *Electroceramics IV*, ed. R. Waser, S. Hoffmann, D. Bonnenberg & Ch. Hoffmann. Augustinus Buchhandlung, Aachen, 1994, pp. 725–732.
13. Dessemond, L., Spectroscopie d'impedance des fissures dans la zircone cubique. Thesis, Grenoble, France, 1992.
14. Landauer, R., Electrical transport and optical properties of inhomogeneous media. In *AIP Conf. Proc.*, ed. J. C. Garland & D. B. Tanner. New York, 1978, pp. 2–45.
15. McLachlan, D. S., Blaszkiewicz, M. & Newnham, R. E., Electrical resistivity of composites. *J. Am. Ceram. Soc.*, **73** (1990) 2187–2203.
16. Bergman, D. J. & Stroud, D., *In Solid State Physics, Vol. 46*. Academic Press, San Diego, 1992, pp. 147–269.
17. Bonanos, N. & Lilley, E., Conductivity relaxations in single crystals of sodium chloride containing Suzuki phase precipitates. *J. Phys. Chem. Solids*, **42** (1981) 943–952.
18. Stroud, D., Milton, G. W. & De, B. R., Analytical model for the dielectric response of brine saturated rocks. *Phys. Review B*, **34** (1986) 5145–5153.
19. Bruggeman, D. A. G., Berechnung verschiedener physikalischer Konstanten von heterogenen Substanzen. *Annal. Physik*, **5** (1935) 636–664.
20. Tomkiewicz, M. & Aurian-Blajeni, B., Impedance of composite materials. *J. Electrochem. Soc.*, **135** (1988) 2743–2747.
21. Bergman, D. J., The dielectric constant of a composite material — a problem in classical physics. *Physics Reports*, **43** (1978) 377–407.
22. Bergman, D. J., Rigorous bounds for the complex dielectric constant of a two-component composite. *Annals of Physics*, **138** (1982) 78–114.
23. McLachlan, D. S., Evaluating the microstructure of conductor–insulator composites using effective media and percolation theories. *MRS Fall Meeting, Boston*, **Abst. # T9.1** 1995 (To be published in the Proceedings).
24. Scott, J. H., Roderick, D. C. & Cunningham, D. R., Dielectric constant and electrical conductivity measurements of moist rock: a new laboratory method. *J. Geophys. Res.*, **72** (1967) 5101–5115.
25. Sen, P. N., Relation of certain geometrical features to the dielectric anomaly of rocks. *Geophysics*, **46** (1981) 1714–1720.
26. Brouers, F., Ramsamugh, A. & Dixit, V. V., A dielectric anomaly in electrolyte-saturated porous alumina ceramics. *J. Mater. Sc.*, **22** (1987) 2759–2766.
27. Fleig, J. & Maier J., Finite element calculations of impedance effects at point contacts. *Electrochim. Acta*, in press.